International Journal of Heat and Fluid Flow 76 (2019) 187–196

Contents lists available at ScienceDirect

International Journal of Heat and Fluid Flow

journal homepage: www.elsevier.com/locate/ijhff

Perturbation threshold and hysteresis associated with the transition to turbulence in sudden expansion pipe flow

Minh Quan Nguyen[a], Mostafa Safdari Shadloo[a], Abdellah Hadjadj[a], Benoit Lebon[1,b], Jorge Peixinho[*,2,b]

[a] CORIA, CNRS-University and INSA of Rouen Normandie, Rouen 76000, France
[b] LOMC, CNRS and Université Le Havre Normandie, Le Havre 76600, France

ARTICLE INFO

Keywords:
Transition to turbulence
Sudden expansion pipe flow
Instability control
Direct numerical simulation (DNS)

ABSTRACT

The complex flow resulting from the laminar-turbulent transition in a sudden expansion pipe flow, with expansion ratio of 1:2, subjected to an inlet parabolic velocity profile and a vortex perturbation, is investigated by means of direct numerical simulations. It is shown that the threshold amplitude for disordered motion is described by a power law scaling, with -3 exponent, as a function of the subcritical Reynolds number. The instability originates from a region of intense shear rate, which results on the flow symmetry breakdown. Above the threshold, several unsteady states are identified using space-time diagrams of the centreline axial velocity fluctuation and their energy. In addition, the simulations show a small hysteresis transition mode due to the reestablishment of the recirculation region in the subcritical range of Reynolds numbers, which depends on: (i) The initial and final quasi-steady states, (ii) the observation time and (iii) the number of intermediate steps taken when increasing and decreasing the Reynolds number.

1. Introduction

The flow through an axisymmetric sudden expansion in a circular pipe is a basic configuration, which occurs in many industrial applications, such as heat exchanger, mixing chamber, combustion chamber, etc. This basic geometry is also used as a building block to model more complex flows such as those occurring in arterial stenoses (Pollard, 1981), pistons (Boughamoura et al., 2003), and transportation pipes (Koronaki et al., 2001), among others. In these applications, the capacity of predicting when the flow will become turbulent is crucial. In the literature, there are many efforts in theoretical analysis (Teyssandiert and Wilson, 1974), experimental explorations (Back and Roschke, 1972; Latornell and Pollard, 1986) and numerical simulations (Macagno and Hung, 1967; Varghese et al., 2007) focusing on this problem, or a similar geometries such as the planar abrupt expansion (Fearn et al., 1990; Xia et al., 1992; Baloch et al., 1995; Bertolotti et al., 2001; Varghese et al., 2007; Tsukahara et al., 2011). More recently, Lebon et al. (2018a) found a new mechanism for periodic bursting of the recirculation region in the flow of a circular pipe with the expansion ratio of 1:2. Yet, a consensus about the sequence of events in the transition from laminar to turbulence seems to be relatively well-established, but the exact value of critical Reynolds number is still not firmly determined, and the different transition scenarios are not yet fully elucidated.

The flow is mainly controlled by the inlet Reynolds number, $Re = \overline{U}d/\nu$, where $\overline{U}$ is the bulk velocity at the inlet, d is the inlet diameter and ν is the fluid kinematic viscosity. In the laminar state, the flow is axisymmetric. As Re increases, the flow starts to break its symmetrical properties but remains steady until $Re = 1139 \pm 10$ as reported in the experiments by Mullin et al. (2009). It should be noted that the onset of symmetry breakdown is at much lower value for the case of channel sudden expansion, as reported to be $Re \approx 40$ by Fearn et al. (1990) and $Re = 216$ by Drikakis (1997). In the sudden circular pipe expansion flows, oscillatory and intermittent bursts were reported to appear at $Re \approx 1567 \pm 16$ by Mullin et al. (2009), $1500 < Re < 1700$ by Sreenivasan and Strykowski (1983), and $Re = 750$ by Latornell and Pollard (1986). Then, the flow develops into localised turbulence at even higher Reynolds numbers (Lebon et al., 2018b).

Recently, a global stability analysis was performed by Sanmiguel-

* Corresponding author.
E-mail address: jorge.peixinho@ensam.eu (J. Peixinho).
[1] IRENav, Institut de REcherche de l'Ecole Navale, 29240 Brest, France
[2] PIMM, CNRS, Arts et Métiers, CNAM, HÉSAM Université, 75013 Paris, France.

https://doi.org/10.1016/j.ijheatfluidflow.2019.01.018
Received 8 November 2018; Received in revised form 16 January 2019; Accepted 22 January 2019

Rojas et al. (2010). They showed that the flow can remain axisymmetric up to $Re \approx 3273$, which is much larger than the value found experimentally. Subsequent simulations by Cliffe et al. (2011) also indicated that the steady supercritical bifurcation point lies at even higher Reynolds numbers, i.e. $Re \approx 5000$. Moreover, a detailed study of transient growth stability was performed by Cantwell et al. (2010). They showed that the sudden expansion amplifies the energy of infinitesimal perturbations up to six orders of magnitude in the inlet, which then decay. The difference between the critical Re in experiments and simulations may be explained by the fact that, in experimental studies, the imperfections of the apparatus have a strong impact on the measured critical Reynolds number. Therefore, the values of critical Reynolds number seem to be dependant both on the perturbation nature and its amplitude. In this case, a numerical simulation with a well-defined finite amplitude perturbation is required to better understand the underlying physics.

Many direct numerical simulations (DNS) on 1:2 expansions were performed before, but with an initial arbitrary velocity field. For example, Tsukahara et al. (2011) showed in a orifice configuration how the turbulent kinetic energy evolves into localised turbulence. Moallemi and Brinkerhoff (2018) used a steady parabolic inflow in a circular pipe expansion and showed the emergence of an instantaneous fluctuating vorticity fields with a maximum near the reattachment point of the recirculation region. The first DNS of finite amplitude perturbation in sudden expansion flow was performed by Sanmiguel-Rojas and Mullin (2012), where many interesting results are reported. They showed that, for a range of Re, the flow in laminar state can be forced to disordered motion when a transverse velocity perturbation is added at the inlet. The minimal amplitude of the transverse velocity perturbation required to initiate disordered motion scaled with $Re^{-0.006}$. This result has an important role in the passive flow control. Now, it is natural to ask if this result is universal? Will another kind of perturbation have the same behaviour? Is the scaling law still valid? The question is crucial especially by knowing that the previous perturbation scheme used by Sanmiguel-Rojas and Mullin (2012) is simply a transverse velocity disturbance in the velocity field. Therefore, it does not satisfy the no-slip boundary condition at the inlet wall. Another interesting result is: When Sanmiguel-Rojas and Mullin (2012) increased and then decreased Re, a hysteresis loop was found for $1450 < Re < 1850$. This point deserves more attention, since in the original work, the process of variation of Reynolds number as well as the physical time of the reported flow state are not specified. Recently, Selvam et al. (2016) presented results on a vortex perturbation but no systematic study of the amplitude threshold and the hysteresis was carried out. One may ask, will the hysteresis occur if Re varies in quasi-static manner? Or will the results change if the observation time is different? In the present study, the authors propose a similar study, but with the vortex disturbance in order to revisit the threshold scaling and the hysteresis loop behaviour.

2. Numerical set-up

The present work focuses on a circular pipe flow with a sudden expansion with the expansion ratio of 1:2. The fluid flow system is solved using Nek5000 (Fischer et al., 2008), a well-validated high-order spectral element code for transitional and fully turbulent flows (Selvam et al., 2015; Ducoin et al., 2017). The governing equations are mass and momentum conservations in an isothermal incompressible limit:

$$\nabla\cdot\mathbf{u} = 0 \tag{1}$$

$$\frac{\partial}{\partial t}\mathbf{u} + \mathbf{u}\cdot\nabla\mathbf{u} = -\nabla p + \frac{1}{Re}\Delta\mathbf{u} \tag{2}$$

where $\mathbf{u}$ is the velocity field, p is the pressure, and t is the physical time. The density of flow is set to unity for simplicity.

The computational domain is axisymmetric as depicted in Fig. 1(b). The region upstream of the expansion is called inlet and has a diameter, d, and a $5d$ length. The downstream region, after the expansion, has a diameter $D = 2d$ and a length $L = 150d$. The whole domain contains 62 300 spectral elements where each element consists of P^3 Gauss–Legendre–Lobatto (GLL) points, P being the polynomial order. $P = 5$, with total number of 7.9 million calculating points, is used for the reported results. Moreover, additional simulations, performed with $P = 6$ (13.5 million GLL points) for showed the laminar recirculation length and the drag coefficient remain essentially the same. A classical set up for the inlet velocity, located at $z = -5d$, is the Hagen–Poiseuille profile, which satisfies the non-slip condition at the inlet wall: $\mathbf{u}^o_{inlet}(r = d/2, z = -5d) = 0$ when $r = \sqrt{x^2 + y^2} = d/2$ and

$$\mathbf{u}^o_{inlet}(x, y, z = -5d) = 2\overline{U}\,[1 - 4(x^2 + y^2)/d^2]\mathbf{e_z}, \tag{3}$$

where ($\mathbf{e_x}$, $\mathbf{e_y}$, $\mathbf{e_z}$) are the three unit vectors of the cartesian base.

In order to initiate turbulence in subcritical Re, a vortex perturbation is added to the inlet parabolic profile (Selvam et al., 2016). This modifies the expression of velocity inlet as:

$$\mathbf{u}_{inlet}(x, y, z = -5d) = \mathbf{u}^o_{inlet} + \mathcal{A}\Omega\begin{pmatrix} -y \\ x \\ 0 \end{pmatrix} = \begin{pmatrix} -\mathcal{A}\Omega y \\ \mathcal{A}\Omega x \\ 2\left[1 - 4\underbrace{(x^2 + y^2)}_{r^2}\right] \end{pmatrix}, \tag{4}$$

where $\mathcal{A}$ and Ω are the amplitude and the intensity of the vortex perturbation, respectively. Ω is defined by: (i) The vortex radius, $R_\Omega = d/4$, (ii) the center (x_Ω, y_Ω) and (iii) the distance from the centerline to the center of the vortex: $r_\Omega = \sqrt{(x - x_\Omega)^2 + (y - y_\Omega)^2}$. Then, the expression of Ω is given by:

$$\Omega = \begin{cases} 1, & r_\Omega \le R_\Omega/2 \\ 8(R_\Omega - r_\Omega)/d, & R_\Omega/2 \le r_\Omega \le R_\Omega \\ 0, & r_\Omega > R_\Omega \end{cases} \tag{5}$$

The position of the vortex is fixed with $x_\Omega = -d/4$ and $y_\Omega = 0$, such as the inlet profile obeys the incompressible, non-slip and non-penetrate boundary conditions. The radius and the position of the vortex, r_Ω, is chosen such that Ω vanishes at the boundary. By injecting $\Omega = 0$ into Eq. (4), one can easily verify that $\mathbf{u}_{inlet}$ vanishes at the boundary as well.

Preliminary tests with a large vortex perturbation on the pipe centreline indicate the required amplitude to initiate turbulence is relatively large. It corresponds to the limit case of the rotating Hagen–Poiseuille flow discharging into a sudden expansion (Miranda-Barea et al., 2015). By positioning the vortex at $(x_\Omega, y_\Omega) = (-d/4, 0)$, the vortex breaks the axial symmetry (Wu et al., 2015) of the flow and deflects the recirculation region. The distribution of $\Omega(x, y)$ can be visualised in Fig. 1(a).

3. Distinction between different states of instabilities

The laminar or turbulent state of a flow can be monitored from the time evolution of the drag coefficient:

$$C_z(t) = \frac{\nu}{\pi d L \overline{U}^2}\int_{z=0}^{L}\int_{\theta=0}^{2\pi}\left[\frac{\partial u_z}{\partial r}\right]_{r=d} r\, d\theta\, dz, \tag{6}$$

where d and $L = 150d$ are the radius and the length of the downstream pipe, respectively. Here $r = \sqrt{x^2 + y^2}$ and $\theta = \arctan(y/x)$ are the positions in the radial and azimuthal direction in the cylindrical coordinate system, respectively.

Table 1 presents a summary of the selected simulations along with parameters: Re, $\mathcal{A}$, initial conditions and observed states. While the laminar state is noted as LS, there exist two unsteady states, US1 and US2, with distinct amplitudes and axial position for the disordered turbulent patch. For LS, C_z is steady, i.e. $dC_z/dt \approx 0$. However, for US, C_z is unsteady and larger than the laminar C_z, i.e. $C_{z,LS} < C_{z,US}$.

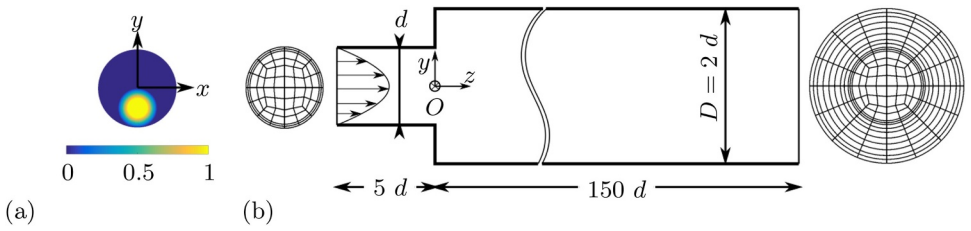

Fig. 1. (a) Axial vorticity of the vortex perturbation ($R_\Omega = d/4$, $(x_\Omega, y_\Omega) = (0, -d/4)$ and $\mathcal{A} = 1$) and (b) Sketch of fluid domain with 2 cross-sections: the inlet and the outlet mesh.

Table 1
Summary of the simulations. Abbreviations: LS: Laminar state and US: Unsteady state. The initial condition could be the Hagen–Poiseuille profile, noted as H-P, or the final times of a past simulation.

Case	Re	$\mathcal{A}$	Initial condition	Remark
1	1100	0	H-P	LS
1a	1100	0.458	1	LS
1b	1100	0.480	1	LS, US2
1c	1100	0.494	1	US1
2	1300	0	H-P	LS
2a	1300	0.2	2	LS
2b	1300	0.239	2	LS, US2
2c	1300	0.385	2	US1
3a	1325	0.2	2a	LS
4a	1350	0.2	3a	LS
5a	1360	0.2	4a	LS, US2
6a	1375	0.2	4a	LS, US2
7a	1400	0.2	6a	LS, US2
7b	1400	0.2	2a	LS, US2
6b	1375	0.2	7b	LS, US2
5b	1360	0.2	6b	LS, US2
4b	1350	0.2	6b	LS, US2
3b	1325	0.2	4b	LS, US2
2b	1300	0.2	3b	LS, US2
8	1600	0	H-P	LS
8a	1600	0.123	8	LS
8b	1600	0.128	8	LS, US2
8c	1600	0.16	8	US1
9a	1700	0.2	9e	US1
9a	2000	0.0773	9	LS
9b	2000	0.0782	9	LS, US2
9c	2000	0.09	9	LS, US2
9d	2000	0.1	9	US2
9e	2000	0.2	9	US1
9f	2000	0.5	9	US1
10a	1700	0.2	3a	US1
L1d	1700	0.2	9e	US1
L2d	1350	0.2	L1d	US2
L3d	1000	0.2	L2d	LS
L2i	1350	0.2	L3d	US2
L1i	1700	0.2	L2i	US1
L3dbis	1325	0.2	L2d	LS

In order to describe the unsteady flow patterns, the axial velocity fluctuations, u_z', at the pipe centreline are obtained by subtracting the instantaneous axial velocity, u_z, to the steady laminar case u_z^0 at the same spatial location:

$$u_z'(0, 0, z, t) = u_z(0, 0, z, t) - u_z^0(0, 0, z), \tag{7}$$

and plotted in a space-time diagram. The reference value u_z^0 is the laminar state with no perturbation, i.e. $\mathcal{A} = 0$. The diagram is constructed from horizontal lines at given times. The colour within the line is the value of u_z' described by 1500 points along the centreline in the z direction at each 100 time-step. The final diagram is the superposition of all computed times with the resolutions of $0.1d$ in space. This diagram is completed by the time evolution of C_z graduated at the top of the diagram. Fig. 2 presents u_z' space-time diagrams and the evolution of drag coefficient, C_z, for four different perturbation amplitudes, $\mathcal{A}$, at $Re = 2000$. The colour intensity in the diagrams increases with the deceleration of the streamwise velocity. The centreline position is typical of this flow configuration and other radial positions close to the centreline would lead to essentially the same qualitative behavior as the localized turbulence fills up the pipe radially. There are two main mechanisms that cause this deceleration. The first one is when the perturbation breaks the flow symmetry down and subsequently the centroid maximum value in the velocity profile is moved away from the centreline. The second mechanism is when the flow becomes disordered, i.e. the instantaneous streamwise velocity fluctuates. Moreover, the mean velocity profile is flattened, which also results in a deceleration in the pipe centreline and is identified in the space-time diagrams by dark (blue) colour and a noisy interface. From the interface and the evolution of C_z, it is clear that the unsteady pattern is closely related to the fluctuations of C_z. For low amplitude disturbance, or low values of $\mathcal{A}$, i.e. $\mathcal{A} \leq 0.09$, depicted in Fig. 2(a) and (b), the disordered turbulent patch is carried downstream, C_z relaminarises for $750 < t < 1000$ and then disordered motion reappears, suggesting an intermittent behaviour. For $\mathcal{A} = 0.2$, depicted in Fig. 2(c), the disordered motion initiated by the perturbation remains unsteady and is labelled US1, as long as the perturbation is applied. Note that the position of the trailing edge of the turbulent patch and C_z fluctuate with time. For even larger $\mathcal{A}$, see e.g. Fig. 2(d), the position of the trailing edge is firmly located at $z \approx 10d$ and is labelled US2.

Typical flow fields, for $Re = 2000$, are shown in Fig. 3. The contour plots present the laminar asymmetric flow pattern, see Fig. 3(a), and the breakup of the recirculation region into localised turbulent patch, see Fig. 3(b) and (c), which can move axially along the downstream section.

In Fig. 4, a summary of the simulation cases is presented in the form of a threshold curve where the boundaries between LS and US2 are shown. Systematically, the US1 is between the LS and the US2 indicating the border between laminar and disordered motion is sensitive to initial conditions. The threshold can be described by a power-law fit: $\mathcal{A} \propto Re^{-3}$, which is much steeper than the value (-0.006) that is reported by Sanmiguel-Rojas and Mullin (2012) indicating that the flow is more and more sensitive as Re increases. Note that the perturbation used by Sanmiguel-Rojas and Mullin (2012) is a transverse velocity (tilt), i.e. an addition of a y-transverse velocity component to the parabolic inlet flow, which creates a velocity discontinuity in the inlet section and at the wall. The effects of the generated shear could depend on the mesh resolution as well as on how the solver interpolates the discontinuity. A recent experimental study from Lebon et al. (2018a,b) has shown a power-law of $Re^{-2.3}$, which is in closer agreement to the present numerical results. In the experiments, several disturbances mechanism were tested: (i) Single, (ii) suction and (iii) periodic in–out or synthetic jet from a hole in the wall. Clearly, a direct comparison between the experiments and the DNS is not straightforward for the reason that the vortex perturbations and the jet disturbances are different. Yet, the effect of the vortex perturbation or the jet disturbance is to break the flow symmetry and distort the recirculation region.

4. Transient growth of unsteady flow patterns

Taking advantage of the time-accurate and 3D opportunities of our DNS results, the unsteady flow patterns are examined. Figure 5(a) presents the space-time diagram for $Re = 1360$ and $\mathcal{A} = 0.2$, corresponding to case 5a in Table 1. The flow experiences several sequences of laminar, oscillatory and disordered motion, as well as

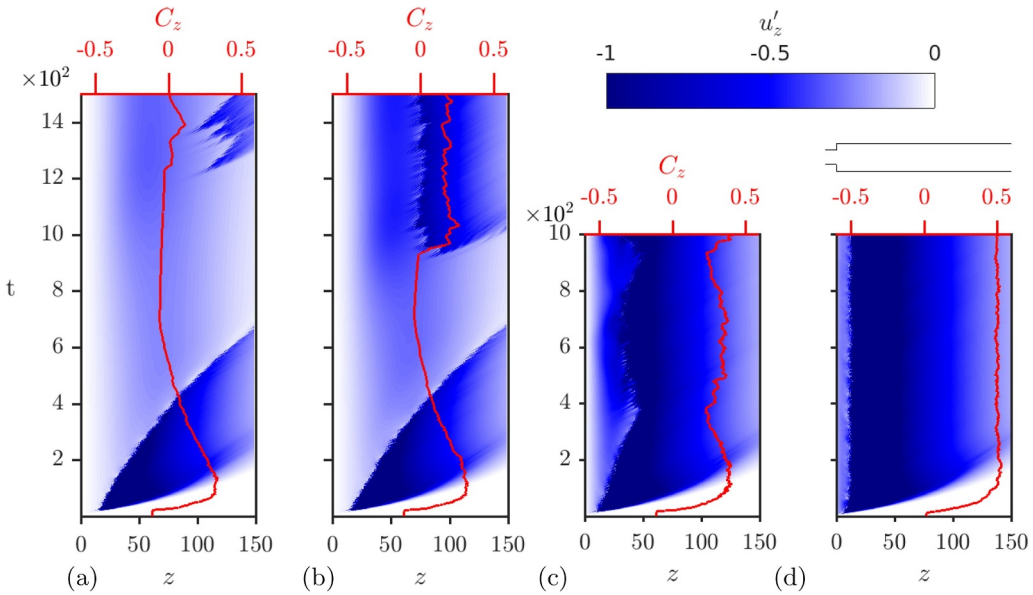

Fig. 2. Space-time diagrams of the centreline perturbed streamwise velocity, u_z', and drag coefficient, C_z, as a (red) line, indicated on the top, for $Re = 2000$ at (a) $\mathcal{A} = 0.0782$, (b) $\mathcal{A} = 0.09$, (c) $\mathcal{A} = 0.2$ and (d) $\mathcal{A} = 0.5$. All the diagrams use the same colour code shown on the top right corner, such that light colour corresponds to laminar flow. The whole pipe section downstream the expansion, up to $z = 150d$, is also sketched in the top right corner below the colour bar.

relaminarisation of the turbulent localised patches. In Fig. 5(b), two profiles of u_z' along the centreline at $t = 1000$ s, before the emergence of a turbulent patch, and at $t = 2500$ s, during a turbulent patch, are presented. The profiles can be divided into three regions. In the first region, $z < 20d$, the flow experiences a gradual deceleration. For $20d < z < 50d$, weak wavy unsteady oscillations are observed. The wavelength is $\approx 2.3d$. In the third region, $z > 50d$, the oscillations decay for $t = 1000$ s, whereas they are considerably amplified for $t = 2500$ s. The fluctuations in the unsteady localised patch become large compared to the oscillations discussed before.

Fig. 6 presents two streamwise velocity fluctuations, u_z', signals, recorded respectively at $z = 40d$ and $z = 80d$ along the pipe centreline. The signals at $z = 40d$ depicted in Fig. 6(a) and (c) have a similar noise amplitude $u_z' \approx 0.1$ and frequency around 0.2 Hz. However, the signals presented in Fig. 6(b) and (d) at $z = 80d$ have a different behaviour, correspond to LS and US2, respectively. Thus, at early stages of development, the differences between the two cases are not particularly striking, so the transition process involves subtle effects. These observations are in disagreement with the transient growth analysis (Cantwell et al., 2010) in the sense that the disturbance generated at the inlet grows while traveling downstream, mainly because of its interactions with the recirculation region. In the current DNS, the present methodology uses finite amplitude perturbation, which can either decay or grow. Furthermore, the perturbation can remain silent or bounded for a long time and then suddenly grow because of the nonlinear interactions between the unsteady flow and the downstream of the recirculation region, where the reattachment point is located.

The unsteady flow pattern can be also analysed by using a Reynolds averaging technique based on a LS domain. The base flow is approximated by taking the average fields during the LS from $t = 1500$ to 1800 s:

$$\overline{\mathbf{u}}(x, y, z) = <\mathbf{u}(x, y, z, t)>_{1500<t<1800} . \tag{8}$$

Then, the unsteady pattern can be expressed using:

$$\mathbf{u}'(x, y, z, t) = \mathbf{u}(x, y, z, t) - \overline{\mathbf{u}}(x, y, z). \tag{9}$$

The amplitude of $\mathbf{u}'(x, y, z, t)$ is small and stays bounded in laminar phase. For convenience, the coordinate system is converted from Cartesian, $\mathbf{u}'(x, y, z, t)$, to cylindrical, $\mathbf{u}'(r, \theta, z, t)$. Next, the Fourier transform of $\mathbf{u}'(r, \theta, z, t)$ in azimuthal direction, noted as $\hat{\mathbf{u}}'$, is

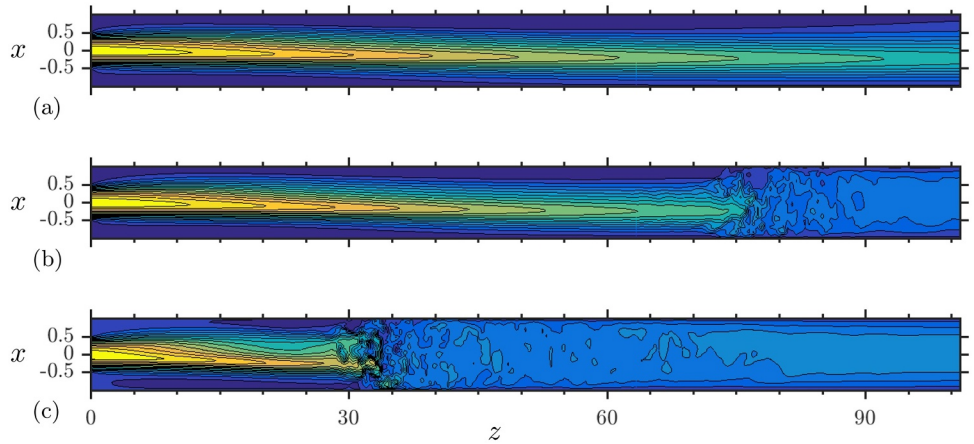

Fig. 3. Contour plot of instantaneous streamwise velocity at $Re = 2000$, $y = 0$ and zoomed into the range of $0 < z < 100d$. (a) LS at $\mathcal{A} = 0.09$, $t = 750$, (b) US2 at $\mathcal{A} = 0.09$, $t = 1250$ and (c) US1 at $\mathcal{A} = 0.2$, $t = 1000$.

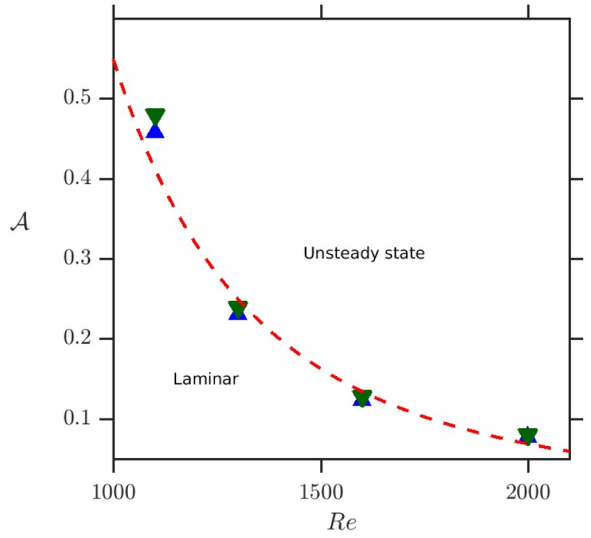

Fig. 4. Critical amplitude, $\mathcal{A}$, of the vortex perturbation as a function of Re. The (green) triangles down indicate US and the (blue) triangles up LS. The (red) dashed line is power-law fit: $\mathcal{A} \propto Re^{-3}$.

computed:

$$\hat{\mathbf{u}}'(r, k_\theta, z, t) = \frac{1}{2\pi}\int_0^{2\pi} \mathbf{u}'(r, \theta, z, t) e^{-2i\pi\theta k_\theta} d\theta, \tag{10}$$

where, the azimuthal modes energy are computed point-wise as:

$$\begin{pmatrix} e_z(r, k_\theta, z, t) \\ e_y(r, k_\theta, z, t) \\ e_z(r, k_\theta, z, t) \end{pmatrix} = \frac{1}{2}\begin{pmatrix} |\hat{u_x'}(r, k_\theta, z, t)|^2 \\ |\hat{u_y'}(r, k_\theta, z, t)|^2 \\ |\hat{u_z'}(r, k_\theta, z, t)|^2 \end{pmatrix}, \tag{11}$$

and the total energy of each azimuthal modes is the sum of all three directions.

From the linear stability point of view, the perturbation $\mathbf{u}'$ could be decomposed into growing and decaying modes. However, in our case, its magnitude stays bounded and fluctuates for a long time, before the transient growth starts and US2 emerges. It suggests there should be a slow growing mode. The observation of the time evolution of all azimuthal modes, over all z, r and k_θ, reveals no steady increasing of energy. Instead, in addition to the regular unsteady pattern, a perturbation appears in the steady zone, $z < 20d$, and evolves into turbulence. A closer look into the time evolution of the perturbation amplitude in the vicinity of transition, for 1900 s $< t <$ 2200 s, is shown in Fig. 7 for an arbitrary value of r, here $r = d/4$, and three different streamwise positions. The other values of r exhibit similar behaviours. The fluctuations of energy in streamwise direction, $e_z(r, k_\theta, z, t)$, or spanwise direction, $e_{xy} = e_x + e_y$, are recorded as a signal in time for given values of z, r and k_θ. The magnitude of the energy of the azimuthal modes is several orders smaller than the streamwise energy. From these signals, a local energy peak in the time-evolution can be observed and is located close to the transition. This peak can be recorded as a time t_p corresponding to the maximum of the energy signal. The values of collected t_p will be a function of spatial positions r, z and the mode k_θ. By comparing the fluctuation patterns, it is found that fluctuations in streamwise direction are approximately two orders of magnitude stronger than the sum of energy fluctuations in the two other spanwise directions in the laminar region, $z < 20d$. However, the gap in the energy levels gets closer at the transition point in the second zone: $z \approx 50d$ and the nonlinear region, in the third zone: $z > 60d$. Another observation is that the position of the energy peaks mainly depends on the streamwise position, z, and seems to be independent of spanwise variables, r and k_θ. For $z \approx 17d$, the peaks start to be observed at $t = 2080$ s.

Fig. 8 presents the contour plots at $z = 17d$ of different streamwise velocity in the cross-sectional plane. It is found that the most intense perturbation in the energy peak appears close to the strongest shear rate position in the streamwise velocity mean profile $\bar{u}_z$, see Fig. 8(b). This suggests the energy peak is related to a shear instability and is independent of the regular unsteady pattern u_z'. The regular unsteady pattern, see Fig. 8(c), is the fluctuation collected before the peak emerges. The latter structure is different from both the peak velocity and the mean flow profile.

Considering the first four modes ($k_\theta \in \{0, 1, 2, 3\}$), as shown in Fig. 7, one can notice the position of local energy peak evolves smoothly and linearly in the streamwise direction in the range of $10d < z < 50d$. This suggests that the energy peak is a perturbation that appears, gets carried downstream by the main flow and amplifies. In Fig. 9(a), the tracking of the local peaks velocity in space, z, and time, t, is shown for all the value of r, where a linear fit of $z/V_0 + c_1$ with c_1 is a constant and $V_0 \approx 0.667$. The error of the tracking process mainly comes from the output frequency of the data and the fluctuation in z direction. All the peaks are found in the range $10d < z < 40d$. It is interesting to mention that the peak evolution tracking in space, z, and

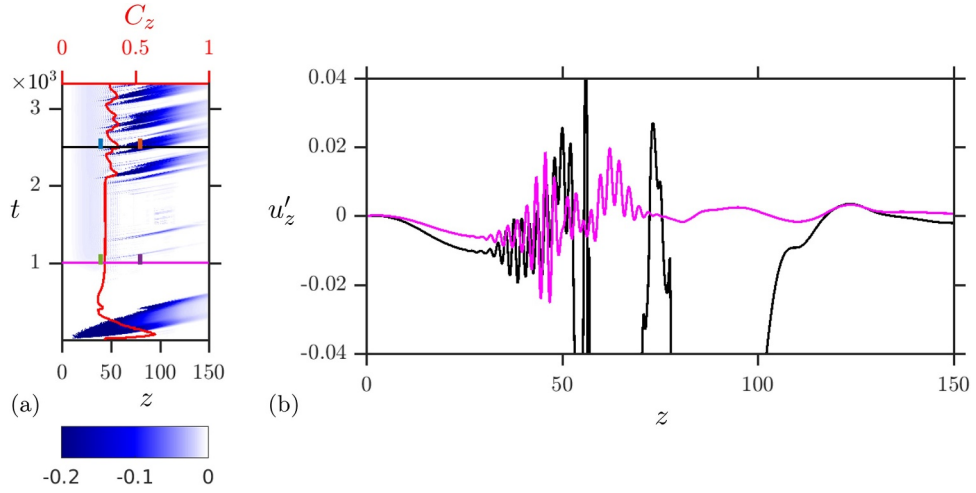

Fig. 5. (a) Space-time diagram for $Re = 1360$ and $\mathcal{A} = 0.2$, corresponding to case 5a. (b) $u_z'(0, 0, z, t)$ profiles along the centreline at $t = 1000$ (LS ▬) and $t = 2500$ (US2 ▬).

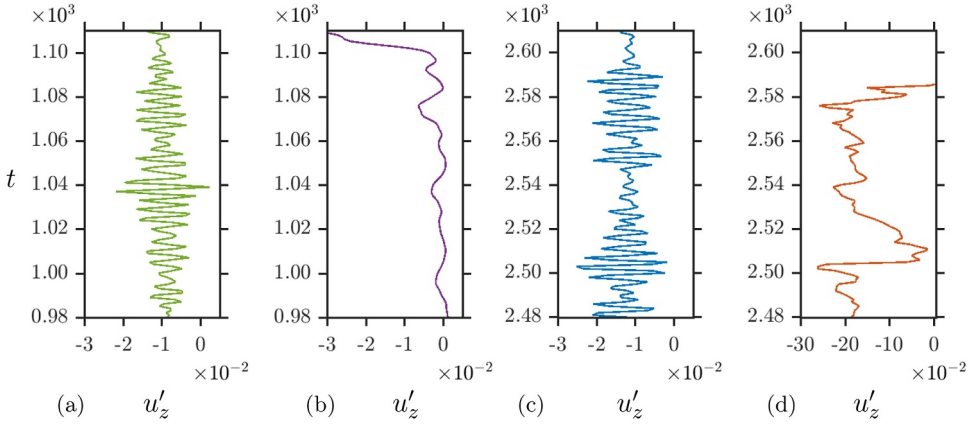

Fig. 6. $u_z'(0, 0, z, t)$ signal over time for $Re = 1360$ and $\mathcal{A} = 0.2$ recorded at $z = 40d$ (a) and $z = 80d$ (b). The time range of (a) and (b) are in LS, whereas the time rage in (c) and (d) are in US2, recorded at $z = 40d$ (c) and $z = 80d$ (d). The time range in this figure are marked with the corresponding colour in Fig. 5(a).

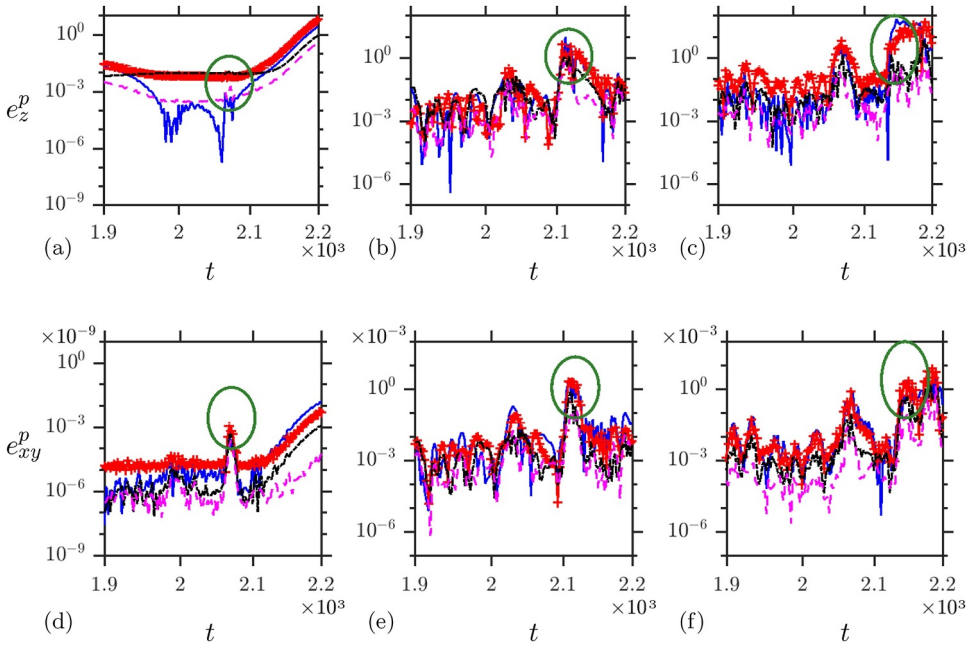

Fig. 7. Time-evolution of the energy of the most relevant azimuthal modes at $r = d/4$ for $Re = 1360$ and $\mathcal{A} = 0.2$. The colour code is: Blue line for the mode 0, red (thick) line for the mode 1, black line for mode 2, and magenta line for mode 3. The three plots in upper row (a,b,c) show the energy of fluctuation pattern in streamwise direction, e_z, and the three plots in the lower row (d,e,f) show the energy of fluctuation pattern in spanwise direction. The three columns correspond to (a,d) $z = 17d$, (b,e) $z = 47d$ and (c,f) $z = 67d$. The (green) circles indicate the peaks of energy.

in time, t, collapse for all the values of spanwise variables (r and k_θ). As a consequence the magnitude of the energy peaks over time grows following a power law as shown in Fig. 9(b). The growth for the first four azimuthal modes takes place until $z \approx 50d$ where the energy saturates. It is noted that the phenomenon of the convective instability is also observed in the numerical simulations of flow over a backward-facing step (see i.e. Blackburn et al., 2008).

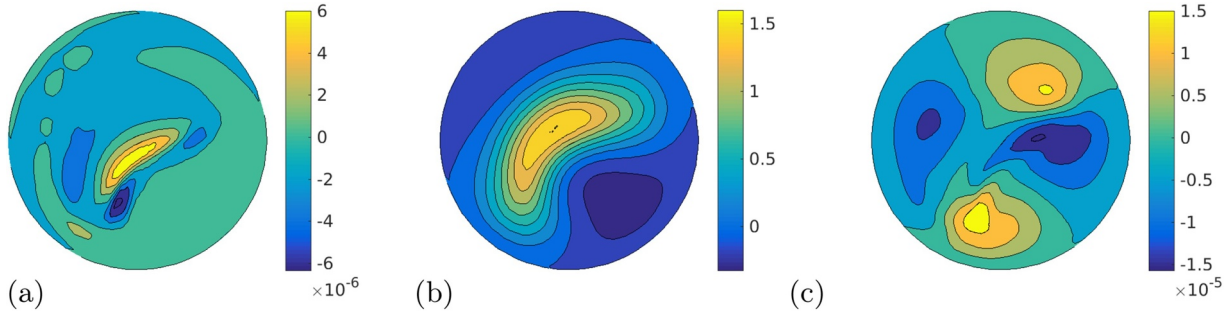

Fig. 8. Contour plot in the cross-sectional plane at $z = 17d$ for $Re = 1360$ and $\mathcal{A} = 0.2$. (a) $u_z^p(z = 17d) = u_z(z = 17d, t_p = 2080) - u_z(z = 17d, t = 2070)$, (b) mean flow: $\bar{u}_z(x, y, z = 17d)$ and (c) regular unsteady pattern that remains bounded over time: $u_z'(x, y, z = 17d, t = 2070)$

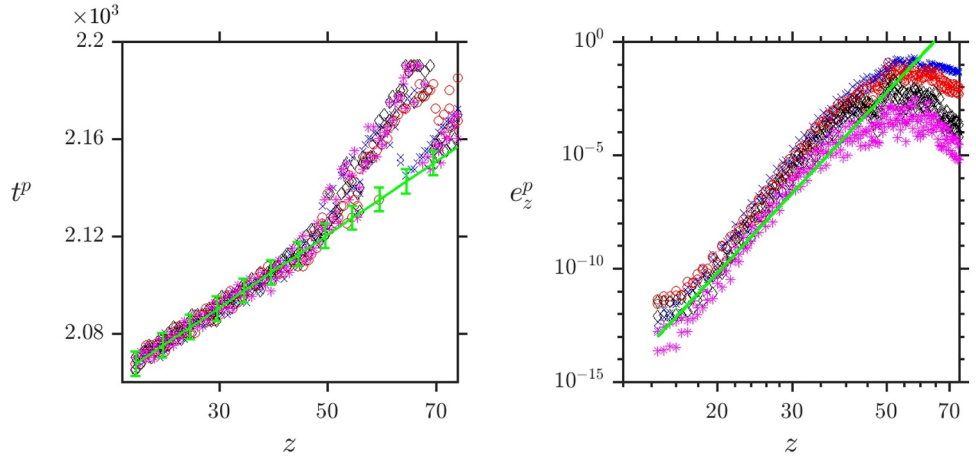

Fig. 9. Tracking position of the energy peak for $Re = 1360$ and $\mathcal{A} = 0.2$. (a) Time and axial position with the scaling represented as a (green) line: $t^p = z/V_0 + c_1$, c_1 is a constant and the different colours represented different radial position. (b) Energy peak amplitude, e_z^p, versus axial position, z, for the first four modes: mode 0 (⊗), mode 1 (○), mode 2 (◇), mode 3 (∗), with the scaling in (green) line $e_z^p = c_2 z^{20}$ where c_2 is a constant.

5. Hysteresis

In general, a hysteresis appears when two flow solutions can exist for the same *Re*. Therefore, the initial conditions and the parameters of the disturbance control the appearance of the two solutions. To test the hysteresic behaviour, two branches of the simulations with *Re* increasing and *Re* decreasing are investigated. The *Re* increasing branch starts from laminar flow, whereas the *Re* decreasing branch begins from an unsteady state, here US2. This approach was also considered by Sanmiguel-Rojas and Mullin (2012) using a transverse velocity disturbance of amplitude δ. Depending on δ and *Re*, a domain of hysteresis was observed. Specifically, for $\delta = 0.001$, the coexistence region was reported for $1475 < Re < 1850$. Moreover, they found that the hysteresis region grows as δ decreases. It is not possible to directly compare the effect of the transverse velocity disturbance with our vortex disturbance because these perturbations are of different nature: the vortex disturbance perturbation introduces rotation, whereas the transverse velocity disturbance introduces a translation to the flow. However, the following results discuss the universality of the hysteresis behaviour. A series of eight simulations were performed, with a fixed amplitude of vortex perturbation, $\mathcal{A} = 0.2$. The initial condition is case 3a with $Re = 1300$. When the simulation time reached 1500 s, the final state is analysed and used as the initial condition for the next run at a higher *Re*. Then, *Re*, is increased with steps of 25, up to $Re = 1400$ (case 4a, 5a, 7a, 8a), as depicted in the space-time diagrams of Fig. 10(*a*). In Fig. 10(*b*), the decreasing *Re* branch is initialised with a laminar state (case 3a), then *Re* is directly increased to 1400 (case 8b) and the decreasing path down to 1300 with a step of 25 (case 7b, 5b, 4b). The simulations from the increasing and decreasing paths are compared for the same *Re*. The results are presented in Fig. 10(*a*) and (*b*) and show minor changes. Looking at the drag coefficient also represented in Fig. 10(*a*) and (*b*), every change in *Re* initiates a peak or a transient increase of C_z corresponding to a disordered patch that propagates and decays downstream. A small hysteresis is found while following this procedure.

Additional simulations were performed using different *Re* steps and a larger range of *Re*. The decreasing branch started with $Re = 2000$. Then *Re*, is decreased to 1700, 1350 and 1000 (simulation L1d, L2d, L3d). The results is compared with the increasing branch which start from $Re = 1000$ then increase to 1350, then 1700 (simulation L3d, L2i, L1i). Again, the results are represented in the form of space-time diagrams, in Fig. 11(*a*) and (*b*). The data show minor differences in the space-time behaviour. However, the drag, C_z, now suggests a small loop of hysteresis.

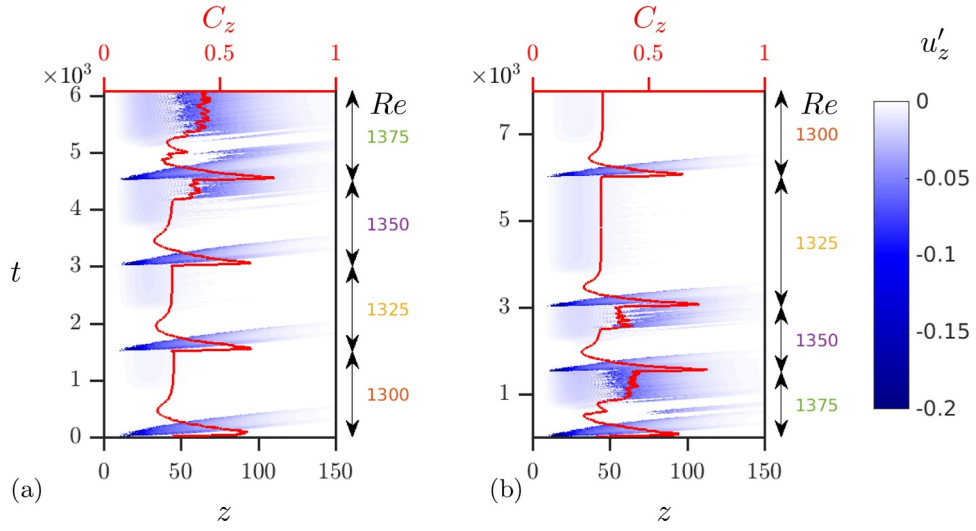

Fig. 10. Hysteresis loop of transitional flows for $\mathcal{A} = 0.2$. (*a*) Space-time diagrams of the increasing *Re*, (cases 3a, 4a, 6a and 7a) and (*b*) the decreasing *Re*, (cases 7b, 6b, 4b and 3b) branches. The diagrams also indicate the value of C_z as a (red) continuous line labeled on the top and the corresponding values of *Re* on the right.

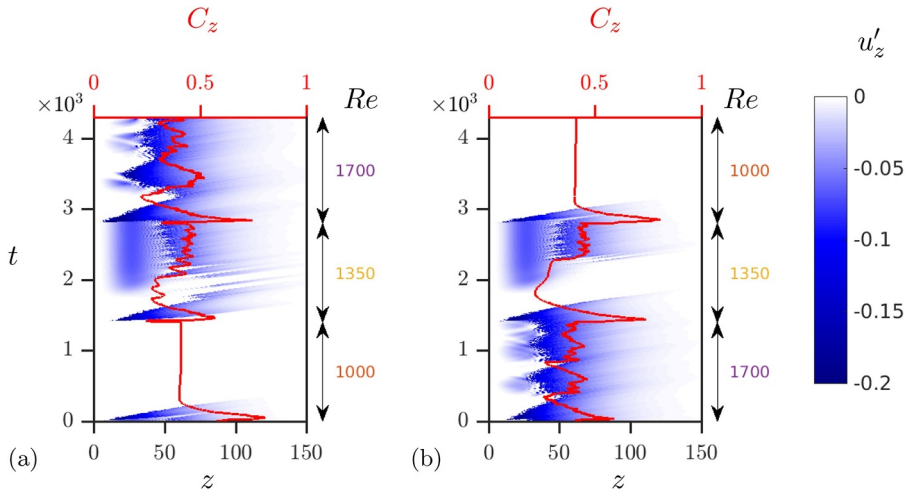

Fig. 11. Hysteresis loop of transitional flows for $\mathcal{A} = 0.2$. (*a*) Space-time diagrams of the increasing *Re* (cases L1d,L2d and L3d) and (*b*) the decreasing *Re* (cases L3d,L2i,L1i) branches. The diagrams also indicate the value of C_z as a (red) continuous line labeled on the top and the corresponding values of *Re* on the right.

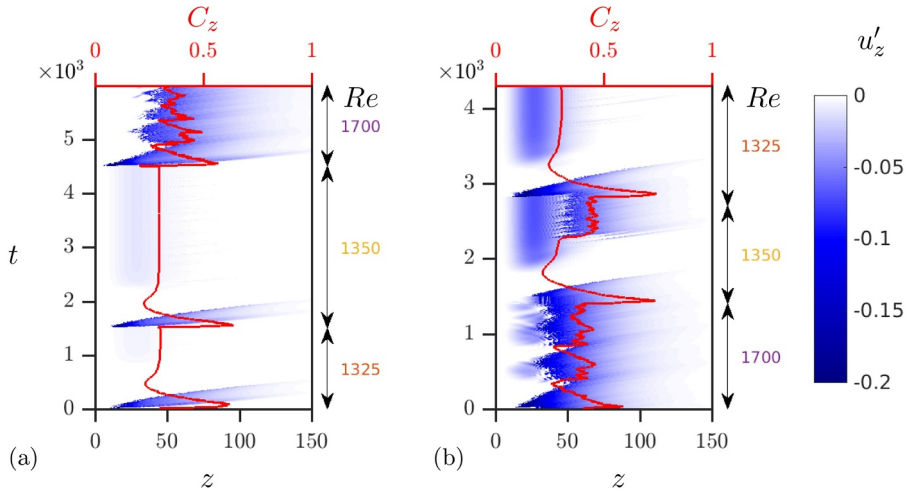

Fig. 12. Hysteresis loop of transitional flows for $\mathcal{A} = 0.5$. (*a*) Space-time diagrams of the increasing *Re* (cases L1d,L2d,L3dbis) and (*b*) the decreasing *Re* (cases 3a, 4a and 10a) branches. The diagrams also indicate the value of C_z as a (red) continuous line and the corresponding value of *Re* on the right.

When comparing two series of simulations, one could notice: in the first loop, with small steps of *Re* ($\Delta Re = 25$), the two cases with $Re = 1350$ are laminar in both increasing and decreasing branches. Whereas, in the second series, with larger steps of *Re* ($\Delta Re = 350$), the two cases with same $Re = 1350$ show US2. The space-time diagram of 4 cases with $Re = 1350$ are extracted in the two series and shown in Fig. 12. The different behaviour of the same *Re* suggests that larger steps of *Re* could eventually trigger the unsteady behaviour and potentially the hysteresis loop sooner than smaller steps.

To quantify the hysteresis behaviour, *S*, the integral of the curve C_z over *Re* for both increasing and decreasing branches is defined:

$$S = \int C_z(Re)dRe. \tag{12}$$

The relative difference, *H*, is defined to quantify the hysteresis behaviour:

$$H = \frac{\Delta S}{\overline{S}}. \tag{13}$$

where ΔS is the difference between two branches and $\overline{S}$ is the mean value. It is noted that in order to observe the hysteresis phenomenon clearly, a specific procedure needs to be implemented. In the decreasing branch, the variation of *Re* should be large enough to avoid the transformation from US1 to US2. On the other hand, in the increasing branch, the variation of *Re* should be small enough to keep the flow laminar. The loops are presented in Fig. 13, with the decreasing branch initiated at $Re = 2000$, then decreasing consecutively to 1700, 1350 and 1325 (simulation L1d, L2d, L3dbis). The increasing branch is initiated at $Re = 1300$ and is then increased consecutively to 1325, 1350 and 1700 (simulation 3a, 4a, 10a). Based on the criteria defined in Eq. (13), this last procedure leads to a hysteresis of $H = 27.87\%$ compared to the two previous loops with the measure of hysteresis are $H = 1.15\%$ and $H = 0.75\%$ respectively. In Fig. 13, C_z is obtained from the last 100 seconds of each case and is plotted against *Re*. The laminar states, $Re = 1325$ and $Re = 1350$, lead to C_z with almost the same value within 0.04%. The unsteady states at $Re = 1375$ and $Re = 1400$ have slightly different final value of C_z within 3% because of the unsteady nature of the flow. The systematic study of all possible steps with extremely long time scales would be a tedious investigation thus beyond the scope of this study. The fact that the hysteresis measure, *H*, increases with the *Re* steps height suggests the hysteresis is related to the re-establishment of the recirculation region.

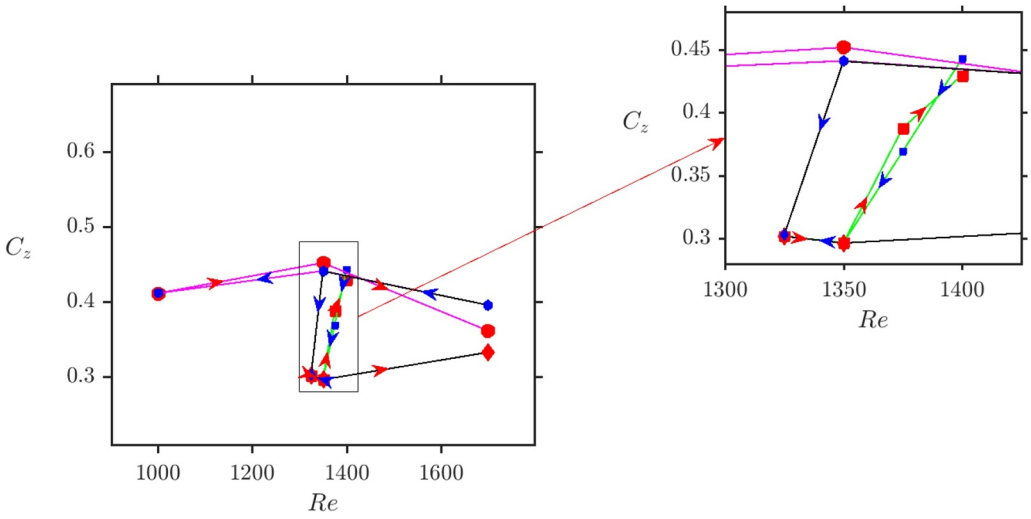

Fig. 13. Hysteresis loop: C_z as a function of Re. The left hand side plot is the global view and the right hand-side plot shows a zoom into to loop. Three sequences of simulations are presented: The cases shown in Fig. 10 in green line with square markers and the cases shown in Fig. 11 in magenta lines with circular markers. In each sequence, the simulations in increasing branch are differentiated with the ones in decreasing branch by the arrows showing the direction of variation of Re. Additionally, the increasing branches are presented with bigger red marker and red arrows, whereas the one in decreasing branch are with smaller blue marker and blue arrows.

6. Conclusion

The results of numerical simulations of the flow through a circular pipe with a sudden expansion have been reported. The expansion ratio is 1:2 and the inlet velocity profile is parabolic together with a finite amplitude vortex perturbation. The spatio-temporal velocity fluctuation have been presented when the perturbation amplitude is larger than the threshold. In the sub-critical range of Reynolds number, the critical threshold scales with Re^{-3} which is consistent with recent experiments (Lebon et al., 2018a; 2018b). The present vortex perturbation, added at the inlet, distorts the flow and the recirculation region before the appearance of disordered motion close to the reattachment point of the laminar recirculation region.

Using the present DNS, it was possible to monitor spatially and temporally the velocity fluctuations, the drag coefficient and the energy of the flow. Furthermore, it was found that the velocity fluctuations in the streamwise direction are dominant, i.e. about two orders of magnitude larger than the transverse flow components. Additionally, a peak of energy fluctuations was observed around to the region of high shear rate close to the point of reattachment of the recirculation region and its amplitude grows exponentially along the axial position of the expansion. Finally, a hysteresis quantification procedure, increasing and decreasing the Reynolds number, indicate a small hysteresis region. Its measure depends on the step and computation time, suggesting a transient effect due to the re-establishment of the recirculation region. In the future, it is planned to extend the present simulations to other types of disturbances and to expansions with various expansion ratio and diverging angles (Lanzerstorfer and Kuhlmann, 2012; Jotkar et al., 2015; Jotkar and Govindarajan, 2019; Kfuri et al., 2017).

The computations were conducted using HPC resources from the Centre Régional Informatique et d'Applications Numériques de Normandie (CRIANN) and from the GENCI/IDRIS. The authors acknowledge financial support of the Agence National de la Recherche (ANR) thought the programme 'Investissement d'Avenir' from the laboratoire d'excellence Energy Materials and Clean Combustion Center (LabEx EMC3). Our work has also benefited from helpful discussions with Ashley P. Willis (University of Sheffield, UK), who suggested this form for the vortex perturbation.

References

Back, L.H., Roschke, E.J., 1972. Shear-layer flow regimes and wave instabilities and reattachment lengths downstream of an abrupt circular channel expansion. J. Appl. Mech. 39, 677.
Baloch, A., Townsend, P., Webster, M.F., 1995. On two- and three-dimensional expansion flows. Comput. Fluids 24, 863.
Bertolotti, C., Deplano, V., Dupouy, P., 2001. Numerical and experimental models of post-operative realistic flows in stenosed coronary bypasses. J. Biomech. 34, 1049.
Blackburn, H.M., Barkley, D., Sherwin, S.J., 2008. Convective instability and transient growth in flow over a backward-facing step. J. Fluid Mech. 603, 271–304.
Boughamoura, A., Belmabroukb, H., Ben Nasrallah, S., 2003. Numerical study of a piston-driven laminar flow and heat transfer in a pipe with a sudden expansion. Int. J. Therm. Sci. 42, 591.
Cantwell, C.D., Barkley, D., Blackburn, H.M., 2010. Transient growth analysis of flow through a sudden expansion in a circular pipe. Phys. Fluids 22 (3), 034101.
Cliffe, K.A., Hall, E.J.C., Houston, P., Phipps, E.T., Salinger, A.G., 2011. Adaptivity and a posteriori error control for bifurcation problems II: Incompressible fluid flow in open systems with Z_2 symmetry. J. Sci. Comp. 47 (3), 389–418.
Drikakis, D., 1997. Bifurcation phenomena in incompressible sudden expansion flows. Phys. Fluids 9, 76.
Ducoin, A., Shadloo, M.S., Roy, S., 2017. Direct numerical simulation of flow instabilities over Savonius style wind turbine blades. Renew. Energ. 105, 374–385.
Fearn, R.M., Mullin, T., Cliffe, K.A., 1990. Nonlinear phenomena in a symmetric sudden expansion. J. Fluid Mech. 211, 595.
Fischer, P.F., Lottes, J.W., Kerkemeier, S.G., 2008. nek5000 Web page. http://nek5000.mcs.anl.gov
Jotkar, M., Govindarajan, R., 2019. Two-dimensional modal and non-modal instabilities un straight-diverging-straight channel flow. Phys. Fluids 31 (014102).
Jotkar, M., Pérez, J.M., Theofilis, V., Govindarajan, R., 2015. Instability mechanisms in straight-diverging-straight channels. Procedia IUTAM 14, 236–245.
Kfuri, S.L., Soares, E.J., Thompson, R.L., Siqueira, R.N., 2017. Friction coefficients for Bingham and power-law fluids in abrupt contractions and expansions. J. Fluids Eng. 139 (021203).
Koronaki, E.D., Liakos, H.H., Founti, M.A., Markatos, N.C., 2001. Numerical study of turbulent diesel flow in a pipe with sudden expansion. Appl. Math. Model. 25 (4), 319–333.
Lanzerstorfer, D., Kuhlmann, H.C., 2012. Global stability of the two-dimensional flow over a backward-facing step. J. Fluid Mech. 693, 1–27.
Latornell, D.J., Pollard, A., 1986. Some observations on the evolution of shear layer instabilities in laminar flow through a sudden expansion. Phys. Fluids 29, 2828.
Lebon, B., Nguyen, M.Q., Peixinho, J., Shadloo, M.S., Hadjadj, A., 2018. A new mechanism for periodic bursting of the recirculation region in the flow through a sudden expansion in a circular pipe. Phys. Fluids 30 (3), 031701.
Lebon, B., Peixinho, J., Ishizaka, S., Tasaka, Y., 2018. Subcritical transition to turbulence in a sudden circular pipe expansion. J. Fluid Mech. 849, 340–354.
Macagno, E.O., Hung, T.K., 1967. Computational and experimental study of a captive annular eddy. J. Fluid Mech. 28, 43.
Miranda-Barea, A., Martínez-Arias, B., Parras, L., Burgos, M.A., del Pino, C., 2015. Experimental study of rotating Hagen–Poiseuille flow discharging into a 1:8 sudden expansion. Phys. Fluids 27 (3), 034104.
Moallemi, N., Brinkerhoff, J.R., 2018. Instability and localized turbulence associated with flow through an axisymmetric sudden expansion. Int. J. Heat Fluid Flow 72, 161–173.
Mullin, T., Seddon, J.R.T., Mantle, M.D., Sederman, A.J., 2009. Bifurcation phenomena in the flow through a sudden expansion in a circular pipe. Phys. Fluids 21 (1), 014110.
Pollard, A., 1981. A contribution on the effects of inlet conditions when modelling stenoses using sudden expansions. J. Biomech. 14 (5), 349–355.
Sanmiguel-Rojas, E., Mullin, T., 2012. Finite-amplitude solutions in the flow through a sudden expansion in a circular pipe. J. Fluid Mech. 691, 201–213.

Sanmiguel-Rojas, E., del Pino, C., Gutiérrez-Montes, C., 2010. Global mode analysis of a pipe flow through a 1:2 axisymmetric sudden expansion. Phys. Fluids 22 (7), 071702.
Selvam, K., Peixinho, J., Willis, A.P., 2015. Localised turbulence in a circular pipe flow with gradual expansion. J. Fluid Mech. 771, R2.
Selvam, K., Peixinho, J., Willis, A.P., 2016. Flow in a circular expansion pipe flow: effect of a vortex perturbation on localised turbulence. Fluid Dyn. Res. 48 (6), 061418.
Sreenivasan, K.R., Strykowski, P.J., 1983. An instability associated with a sudden expansion in a pipe flow. Phys. Fluids 26, 2766.
Teyssandiert, R.G., Wilson, M.P., 1974. An analysis of flow through sudden enlargements in pipes. J. Fluid Mech. 64, 85.
Tsukahara, T., Kawase, T., Kawaguchi, Y., 2011. DNS of viscoelastic turbulent channel flow with rectangular orifice at low Reynolds number. Int. J. Heat Fluid Flow 32 (3), 529–538.
Varghese, S.S., Frankel, S.H., Fischer, P.F., 2007. Direct numerical simulation of stenotic flows. Part 1. Steady flow. J. Fluid Mech. 582, 253.
Wu, X., Moin, P., Adrian, R.J., Baltzer, J.R., 2015. Osborne Reynolds pipe flow: Direct simulation from laminar through gradual transition to fully developed turbulence. PNAS 112 (26), 7920–7924.
Xia, Y., Callaghan, P.T., Jeffrey, K.R., 1992. Imaging velocity profiles: Flow through an abrupt contraction and expansion. AIChE J. 38, 1408.